Journal of The Electrochemical Society, **154** (2) B218-B228 (2007)
0013-4651/2006/154(2)/B218/11/$20.00 © The Electrochemical Society

Probing Liquid Water Saturation in Diffusion Media of Polymer Electrolyte Fuel Cells

Hyunchul Ju, Gang Luo, and Chao-Yang Wang*,z

Electrochemical Engine Center and Department of Mechanical and Nuclear Engineering, The Pennsylvania State University, University Park, Pennsylvania 16802

Neutron radiography (NR) was intended to visualize the accumulation and distribution of product water inside diffusion media (DM) in a polymer-electrolyte fuel cell (PEFC). However, the two-dimensional NR technique is unable to separate anode water from cathode water and resolve the liquid water distribution along the cell thickness, two pieces of information strongly needed to characterize the level of cathode DM flooding or anode dry-out. In this paper, NR data analysis is performed for the first time in the context of a three-dimensional two-phase PEFC model. The numerical study illustrates the difficulty in NR data analysis where the major concern originates from the separation of liquid water in the cathode DM from the water in thick membranes, or from liquid water in the anode DM for the thin membrane case. In addition, the two-phase simulation results show that the calculated amount of water according to NR conditions is well within the range measured by NR experiments in the literature, demonstrating the validity of the present two-phase model. A concern is raised whether the two-dimensional NR technique is suitable for studying water management, which generally requires separation of water between the anode and cathode.
 [DOI: 10.1149/1.2401034]

Manuscript submitted July 18, 2006; revised manuscript received September 8, 2006. Available electronically December 26, 2006.

While increasing oil prices and environmental concerns have become pressing issues worldwide, the polymer-electrolyte fuel cell (PEFC) has received great attention as a promising future energy converter. Despite enormous progresses in PEFC technology for the last decade, several challenges remain before its potential can be realized. One of these is related to flooding phenomena. Due to the presence of liquid water inside a PEFC where the catalyst layer (CL), porous diffusion media (DM), and even gas channel (GC) can be flooded, thereby impeding transport of reactants and oxygen reduction reaction and finally resulting in significant deterioration in cell performance and durability. To resolve the issue, substantial efforts have been made to study flooding phenomena and related two-phase transport inside PEFCs. A number of two-phase PEFC models published in the literature are based on two-phase transport in porous media driven by capillary action, focusing on electrode and DM flooding.[1-18] An overview was provided by Wang.[19] Some of them further analyzed the effects of multi-layer DMs, composed of two or more layers of porous materials having different pore sizes and/or wetting characteristics.[4,7,12,16] Nonisothermal, two-phase transport effects were also investigated[3-5,9,15,17] and transient aspect on liquid water distribution.[2,14,18]

Simultaneously, various experimental techniques for investigation of flooding phenomena have been developed. Optical visualization using transparent cells has been widely employed to study complex mechanisms of liquid water transport in channels, such as droplet formation, growth, and detachment from DM surfaces (hydrophobic), droplet interaction with channel side walls (hydrophilic), as well as development of liquid film on channel walls or channel clogging.[20-24] While optical visualization is capable of visualizing two-phase flow phenomena with high spatial and temporal resolutions in an operating fuel cell, the observable region is limited to flow channels. On the other hand, neutron imaging has been considered as a diagnostic tool to visualize and quantify water accumulation inside an opaque DM because neutron beams are exceptionally attenuated through the hydrogen nuclei contained material (i.e., water) but easily penetrate common materials used in PEFCs, such as carbon. Therefore, a two-dimensional neutron radiograph (NR) can be obtained, resulting from high- and low—attenuations of neutrons passing through the PEFC components. The neutron imaging technique was first employed as a fuel cell experimental tool by Bellows et al.[25] Using 500 μm thick membrane of four bonded layers of Nafion 117 and directing neutron beams from the side, they measured water content distribution in the membrane and investigated the response of membrane water content to various feed gas humidity and current density conditions. Satija et al.[26] utilized neutron radiography to estimate water flooding in operating fuel cells. By applying an image masking technique, they attempted to further differentiate between water accumulation in the anode channel, cathode channel, and cathode DM and concluded that most of the water exists on the cathode side of the cell. However, their masking analysis is only valid under the assumption that the anode DM is absent of water and thus all water in DM is necessarily located in the cathode side. Furthermore, their NR data analysis ignored the amount of water present in the membrane, even when the membrane is quite thick (90 μm) and thereby a significant portion of the water is expected in the membrane (amounts to 50% according to an analysis presented later). Kramer et al.[27] performed neutron radiographic measurements and quantified the amount of liquid water under the current collecting lands with the maximum thickness of liquid water film around 110 μm (roughly corresponding to 11 mg/cm^2 of water mass) near the outlet region, based on a 300 μm thick cathode DM. Zhang et al.[28] further investigated the influence of the flowfield materials and DM on liquid accumulation in PEFCs. They showed lower water accumulation with the gold-coated aluminum flowfield rather than the graphite flowfield and also proved that the cloth-type DM is superior to the paper-type DM for liquid water removal from a cell. Recently, Hickner et al.[29] focused on examining the dynamic response of liquid water under a step change in current density using NR where much slower responses of liquid water were observed, ranging from 300 to 600 s. In addition, they observed that water accumulation increases with increasing current density up to 0.65 A/cm^2 but starts to decline if current density further increases from 0.65 to 1.25 A/cm^2. They concluded that the experimental trend is due to strong thermal effects in the high current density range.

While the above described NR works were concerned with water distribution in DM, Pekula et al.[30] investigated two-phase flow in GCs using NR. They emphasized that a significant amount of liquid water is accumulated in the anode GC at the low current density (0.05 A/cm^2) and also estimated a liquid droplet velocity that amounted to be roughly one order of magnitude smaller than the reactant gas flow.

Although NR has received much interest due to the high sensitivity of neutron beams to water, the two-dimensional radiographs do not resolve the liquid water profile along the cell thickness. In fact, only the amount of liquid water in the cathode catalyst layer and DM is of interest in studies of cathode flooding that limits oxygen transport to catalyst sites. On the other hand, although numerous two-phase PEFC models have been presented in the literature, their prediction of liquid saturation (i.e., the volume fraction of

* Electrochemical Society Active Member.
z E-mail: cxw31@psu.edu

Table I. Two-phase steady state PEFC model: conservation equations.

Conservation equations		
Mass	$\nabla \cdot (\rho \vec{u}) = S_m$	[1]
Momentum	Flow Channels (Navier-Stokes Eqs.): $\frac{1}{\varepsilon^2} \nabla \cdot (\rho \vec{u}\vec{u}) = -\nabla p + \nabla \cdot \tau$	[2]
	Porous media (Darcy's Eqs.): $\rho \vec{u} = -\frac{K}{\nu} \nabla p$	[3]
Species	$\nabla \cdot (\gamma_i \rho m_i \vec{u}) = \cdot \lfloor \rho^g D_i^{g,eff} \nabla (m_i^g) \rfloor + \nabla \cdot \lfloor (m_i^g - m_i^l) \vec{j}^l \rfloor + S_i$	[4]
	Water transport in the membrane: $\nabla \cdot \left(\frac{\rho^{mem}}{EW} D_w^{mem} \nabla \lambda \right) M_w - \nabla \cdot \left(n_d \frac{I}{F} \right) M_w + \nabla \cdot \left(\frac{K^{mem}}{\nu^l} \nabla P^l \right) = 0$	[5]
Charge	Proton transport: $\nabla \cdot (\kappa^{eff} \nabla \Phi_e) + S_\Phi = 0$	[6]
	Electron transport: $\nabla \cdot (\sigma^{eff} \nabla \Phi_s) - S_\Phi = 0$	[7]

liquid water filled pores) ranges from a few percent to higher than ninety percent and there exists no direct validation of these two-phase models against water distribution data. Therefore, it is of great value to comparatively study two-phase PEFC models with the NR experimental technique.

In this work, we apply a two-phase PEFC model developed at ECEC to simulate NR experiments. The purpose of this numerical study is threefold—to compare the present two-phase PEFC model against NR data available in the literature for preliminary model validation beyond current distribution data,[31] to estimate the relative portion of liquid water in cathode DM from the total water measurable by NR under various cell designs and operating conditions, and to elucidate advantages and disadvantages of the NR technique in providing useful data for a rigorous validation of two-phase models and a basic understanding of cathode flooding.

In the following, a two-phase, multidimensional PEFC model is first presented, along with a brief description of the model assumptions, conservation equations and corresponding source/sink terms in the various PEFC components. Then, a method to calculate the total liquid water thickness or area-specific mass that corresponds directly to an NR experiment is defined and numerical simulations are carried out and their results discussed. Finally, major conclusions about the NR numerical study are summarized.

Two-Phase Model

The two-phase PEFC model used for the numerical study is based on the multiphase mixture (M^2) model developed by Wang and Cheng.[32] While the M^2 model is mathematically equivalent to classical two-fluid models without invoking any additional approximations, one significant advantage of this model should be mentioned here, particularly for practical PEFC operating conditions where the dry-to-wet transition often occurs inside a DM due to low-humidity inlet operation, as well as for special operations such as start-up (where the evaporation front forms and propagates through as the cell increases its temperature). The dry-to-wet transition can be well handled by the M^2 model because it has no need for tracking phase interfaces and thus simplifies the numerical complexity of two-phase flow and transport simulations. This fact renders the M^2 model a suitable and widely adopted two-phase modeling approach for PEFCs.[1,3,11,13,17] The reader is referred to Luo et al.[33] for a detailed explanation of the nature of dry-to-wet transition under practical PEFC operations.

Model assumptions.— Utilizing the M^2 formulation for two-phase transport, the present two-phase PEFC model makes the following assumptions—ideal gas mixtures, laminar flow due to small flow velocities, isotropic and homogeneous porous DM, characterized by an effective porosity and a permeability, and two-phase mist flow (i.e., homogeneous flow) in GCs assuming that tiny droplets exist and travel with the gas velocity inside the GCs. The last assumption is made to facilitate the present analysis for liquid water accumulation inside DM over the land only as well as to be mathematically tractable without resorting to a sophisticated two-phase channel flow model.

Conservation equations.— With the above assumptions, the two-phase PEFC model is governed by conservation of mass, momentum, species, and charge under isothermal conditions chosen to simplify the numerical analysis and dramatize the liquid water formation of special interest in the present study. The energy equation is thus ignored. The conservation equations are listed in Table I and have been fully discussed elsewhere.[11,13] To close the equation set, one needs the ideal gas law that describes the gas mixture density varying with its compositions (here, mass fractions). That is

$$\rho^g = \left(\frac{P}{R_u T} \right) \frac{1}{\sum_i \frac{m_i^g}{M_i}} \quad [14]$$

The two-phase mixture density and velocity in M^2 model are given by[32]

$$\rho = \rho^l \cdot s + \rho^g \cdot (1 - s) \quad [15]$$

$$\rho \vec{u} = \rho^l \vec{u}^l + \rho^g \vec{u}^g \quad [16]$$

where s and $(1 - s)$ denote the volume fraction of the open pore spaces occupied by liquid and gas phases, respectively.

In the momentum equations in Table I, note that Darcy's law is used to describe two-phase flow through a porous medium with a relative permeability, k_r^k, introduced. The relative permeability of an individual phase is assumed to be proportional to the phase saturation, raised to the fourth power, i.e.,

$$k_r^l = s^4, \quad k_r^g = (1 - s)^4 \quad [17]$$

In addition, the multiphase mixture kinematic viscosity and the mobility of each phase are defined as[32]

$$\upsilon = \left(\frac{k_r^l}{\nu^l} + \frac{k_r^g}{\nu^g} \right)^{-1} \quad [18]$$

$$\lambda^l = \frac{k_r^l}{\nu^l} \upsilon \quad \lambda^g = 1 - \lambda^l \quad [19]$$

where ν^g is the kinematic viscosity of a gas mixture varying with gas compositions[34]

Table II. Two-phase steady state PEFC model: source/sink terms.

Source/sink terms		
Mass	In the CLs: $S_m = \Sigma_i S_i + M_w \nabla \cdot \left(D_w^{mem} \frac{\rho^{mem}}{EW} \nabla \lambda \right)$	[8]
Species	For water in CLs: $S_i = M_i \left[- \nabla \cdot \left(\frac{n_d}{F} I \right) - \frac{s_i j}{nF} \right]$ For other species in CLs: $S_i = -M_i \frac{s_i j}{nF}$	[9]
Charge	In the CLs: $S_\Phi = j$	[10]
	$\sum_k s_i M_i^z = ne^-$, where $\begin{cases} M_i \equiv \text{chemical formula of species } i \\ s_i \equiv \text{stoichiometry coefficient} \\ n \equiv \text{number of electrons transferred} \end{cases}$	[11]
Electrochemical reactions	Hydrogen Oxidation Reaction (HOR) in anode side: $H_2 - 2H^+ = 2e^-$	[12]
	Oxygen Reduction Reaction (ORR) in cathode side: $2H_2O - O_2 - 4H^+ = 4e^-$	[13]

$$\upsilon^g = \frac{\mu^g}{\rho^g} = \frac{1}{\rho^g} \sum_{i=1}^{n} \frac{x_i \mu_i}{\sum_{j=1}^{n} x_j \Phi_{ij}}, \quad \text{where}$$

$$\Phi_{ij} = \frac{1}{\sqrt{8}} \left(1 + \frac{M_i}{M_j} \right)^{-1/2} \left[1 + \left(\frac{\mu_i}{\mu_j} \right)^{1/2} \left(\frac{M_j}{M_i} \right)^{1/4} \right] \quad [20]$$

and

$$\mu_i, [N \cdot s/m^2] = \begin{cases} \mu_{H_2} = 0.21 \times 10^{-6} T^{0.66} \\ \mu_w = 0.00584 \times 10^{-6} T^{1.29} \\ \mu_{N_2} = 0.237 \times 10^{-6} T^{0.76} \\ \mu_{O_2} = 0.246 \times 10^{-6} T^{0.78} \end{cases}$$

T in Kelvin

The general form of species equation shown in Eq. 4 is derived from the fact that all species mass fractions sum up to be unity. The first term on the right-hand side of the species equation represents the net Fickian diffusion fluxes within a gas phase. Species diffusivity in the gas mixture, D_i^g is defined as follows, so that summation of interspecies diffusion within the gas phase is equal to zero[34]

$$D_i^g = \frac{1 - x_i}{\sum_{\substack{j \neq i \\ j=n}} \frac{x_j}{D_{i,j}}}, \quad \text{where } D_{i,j} = \frac{1.013 \cdot 10^{-7} \cdot T^{1.75}}{p \cdot (\chi_i^{1/3} + \chi_j^{1/3})^2} \cdot \left(\frac{1}{M_i} + \frac{1}{M_j} \right)^{1/2} \quad [21]$$

where $\chi_{H_2} = 7.07$, $\chi_w = 12.7$, $\chi_{N_2} = 17.9$, $\chi_{O_2} = 16.6$.

Note that the gas phase diffusion coefficient for a porous medium is an effective one, modified via Bruggeman correlation[35] to account for the effects of porosity and tortuosity of the porous medium. In the two-phase zone, the gas diffusion coefficient must be further modified because the liquid water also occupies open pore spaces. As a result, the effective gas diffusivity, $D_i^{g,eff}$ in the two-phase region is a function of both porosity, ε, and liquid saturation, s. That is

$$D_i^{g,eff} = [\varepsilon(1 - s)]^n D_i^g \quad [22]$$

The second term on the right-hand side in Eq. 4 is due to the relative motion between both gas and liquid phases where a diffusive mass flux of each phase relative to the whole multiphase mixture is defined. The diffusive mass flux of liquid phase, $\vec{j}^l$ is expressed as a function of capillary pressure, P_c such that[32]

$$\vec{j}^l = \rho^l \vec{u}^l - \lambda^l \rho \vec{u} = \frac{K}{\nu} \lambda^l \lambda^g \nabla P_c \quad [23]$$

The capillary pressure, P_c, defined as the difference between gas and liquid pressures, can be expressed as function of porosity, ε, permeability, K, and contact angle, θ of the porous medium as follows[32]

$$P_c = P^g - P^l = \sigma \cos\theta \left(\frac{\varepsilon}{K} \right)^{1/2} J(s) \quad [24]$$

where Leverett function, $J(s)$, denotes the dimensionless capillary pressure which can be expressed for both hydrophobic and hydrophilic porous layers as[6]

$$J(s) = \begin{cases} 1.417(1 - s) - 2.120(1 - s)^2 + 1.263(1 - s)^3 & \text{if } \theta_c < 90^\circ \\ 1.417s - 2.120s^2 + 1.263s^3 & \text{if } \theta_c > 90^\circ \end{cases} \quad [25]$$

On the left-hand side of the species equation, Eq. 4, there is the advective term, in which the advection correction factor, γ_i is given by[32]

$$\gamma_i = \frac{\rho(\lambda^l m_i^l + \lambda^g m_i^g)}{(s\rho^l m_i^l + (1 - s)\rho^g m_i^g)} \quad [26]$$

Therefore, species, i, is advected by a modified velocity, $\gamma_i \vec{u}$, rather than the original mixture velocity, $\vec{u}$. On the other hand, Eq. 5 represents water transport across the membrane, driven by three mechanisms: diffusion due to the water content gradient, electro-osmotic drag due to the protonic flux, and hydraulic permeation due to the liquid pressure gradient.[12]

Source terms and physicochemical relations.— In Table I, S_m, S_i, and S_Φ denote their corresponding source/sink terms for mass, species, and charge, respectively, and are summarized in Table II. Those source terms result from the electrochemical reactions, the hydrogen oxidation reaction (HOR) in the anode CL (Eq. 12) and oxygen reduction reaction (ORR) in the cathode CL (Eq. 13), respectively, which are represented by kinetic expressions as follows

$$\text{HOR in anode CL} \quad j = (1-s)^{n_c} a i_{0,a}^{ref} \left(\frac{C_{\mathrm{H}_2}}{C_{\mathrm{H}_2,ref}} \right)^{1/2} \left(\frac{\alpha_a + \alpha_c}{R_u T} F\eta \right) \tag{27}$$

$$\text{ORR in cathode CL} \quad j = -(1-s)^{n_c} a i_{o,c}^{ref} \left(\frac{C_{\mathrm{O}_2}}{C_{\mathrm{O}_2,ref}} \right)^{3/4} \exp\left(-\frac{\alpha_c}{R_u T} F\eta \right) \tag{28}$$

where $(1-s)^{n_c}$ is to approximate the effect of decreasing electrochemically active catalyst sites due to the presence of liquid water in the CLs.

The surface overpotential in Eq. 27 and 28 is defined by

$$\text{HOR in anode CL} \quad \eta = \phi_s - \phi_e \tag{29}$$

$$\text{ORR in cathode CL} \quad \eta = \phi_s - \phi_e - U_o \tag{30}$$

where the thermodynamic equilibrium potential between the cathode and anode is given by[36]

$$U_o = 1.23 - 0.9 \times 10^{-3}(T - 298.15) \tag{31}$$

In Table II, a nonzero mass source/sink in the mass conservation equation, S_m, arises from the summation of all species equations. More detailed descriptions of the mass source/sink can be found in Wang and Wang[37] and Wang.[19]

The transport properties of electrolytes are correlated with the water content of the membrane, λ, which is in turn a function of the water activity, a, as follows[38]

$$a = \frac{C_w^g R_u T}{P_{sat}} \tag{32}$$

$$\lambda = \begin{cases} \lambda^g = 0.043 + 17.81a - 39.85a^2 + 36.0a^3 & \text{for } 0 < a \leqslant 1 \\ \lambda^l = 22 \end{cases} \tag{33}$$

The electro-osmotic drag coefficient, n_d, water diffusion coefficient in the membrane, D_w^{mem}, and the proton conductivity in the membrane, κ, are given by Springer et al.[38]

$$n_d = \frac{2.5\lambda}{22} \tag{34}$$

$$D_w^{mem} = \begin{cases} 2.692661843 \cdot 10^{-10} & for\ \lambda \leqslant 2 \\ \{0.87(3-\lambda) + 2.95(\lambda-2)\} \cdot 10^{-10} \cdot e^{(7.9728-2416/T)} & for\ 2 < \lambda \leqslant 3 \\ \{2.95(4-\lambda) + 1.642454(\lambda-3)\} \cdot 10^{-10} \cdot e^{(7.9728-2416/T)} & for\ 3 < \lambda \leqslant 4 \\ (2.563 - 0.33\lambda + 0.0264\lambda^2 - 0.000671\lambda^3) \cdot 10^{-10} \cdot e^{(7.9728-2416/T)} & for\ 4 < \lambda \leqslant \lambda_{a=1}^g \end{cases} \tag{35}$$

$$\kappa = (0.5139\lambda - 0.326)\exp\left[1268\left(\frac{1}{303} - \frac{1}{T} \right) \right] \tag{36}$$

The present two-phase PEFC model described above is numerically implemented with a commercial computational fluid dynamics (CFD) package, STAR-CD, based on its user-coding capability.[39]

Calculation of water mass corresponding to NR experiments.— NR detects a two-dimensional distribution of total water integrated across the entire cell thickness. Thus, to be comparable, the local water distribution predicted by the present PEFC model must be integrated through all PEFC components in the thru-plane direction. The amount of water mass in the unit of mg/cm^2 for all PEFC components can be computed as follows

$$\text{GCs:} \quad wm_{GC} = \int \rho^l s + (1-s)\rho^g m_w^g dx \tag{37}$$

$$\text{DM:} \quad wm_{DM} = \varepsilon_{DM} \int \rho^l s + (1-s)\rho^g m_w^g dx \tag{38}$$

$$\text{CLs:} \quad wm_{CL} = \varepsilon_e \int M_w \frac{\rho^{mem}\lambda}{EW} dx + \varepsilon_{CL} \int \rho^l s + (1-s)\rho^g m_w^g dx \tag{39}$$

$$\text{Membrane:} \quad wm_{mem} = \int M_w \frac{\rho^{mem}\lambda}{EW} dx \tag{40}$$

where x is the thru-plane distance. Hence, the total water mass of the entire cell as measured by NR is simply the sum of water mass in all components, i.e.,

$$\text{Total water mass:} \quad wm_t = wm_{GC} + wm_{DM} + wm_{CL} + wm_{mem} \tag{41}$$

Results and Discussion

For a numerical study, the two-phase PEFC model presented in the preceding section is applied to a single straight channel cell, as schematically shown in Fig. 1 with its mesh configuration. Cell dimensions and parameters are listed in Table III and the relevant physical properties are summarized in Table IV. It is seen from Fig. 1 and Table III that low humidified (75%) hydrogen and air gases are fed into the anode and cathode inlets, respectively, under the counter-flow configuration. The counter-flow of anode and cathode gases is typical of practical PEFC stacks because it ensures more uniform membrane hydration and thus better performance.[40]

Figure 2 shows liquid saturation and liquid/gas velocity distributions in both anode and cathode DMs. First, it is seen in the liquid saturation distribution, Fig. 2a, that the dry-to-wet transition occurring inside each DM due to the low-humidity inlet gas. The liquid velocity in Fig. 2b, roughly three orders of magnitude smaller than the gas velocity in Fig. 2c, is directed from high liquid saturation regions (under the lands) to low ones (under the channels) and vanishes at the evaporation front. On the other hand, the gas flow in Fig. 2c is opposite to the liquid flow in the two-phase zone, due to the capillary-induced gas-liquid counter-flow. Also, oxygen in the cathode DM or hydrogen in the anode DM is consumed in the CL reaction area, generating a gas flow from the channel toward the land along the in-plane direction and toward the CL along the thru-plane direction. Note that in Fig. 2c that the gas flow is primarily along the in-plane direction. Based on Fig. 2c, Peclet number for gas transport along the in-plane direction can be roughly estimated to be unity ($Pe = V^g \delta_{land\text{-}channel} / D^g \approx 10^{-3} \times 10^{-3}/10^{-6} = 1$), implying that both convection and diffusion are significant for gas transport in the DM along the in-plane direction.

Liquid water saturation distributions at both anode and cathode

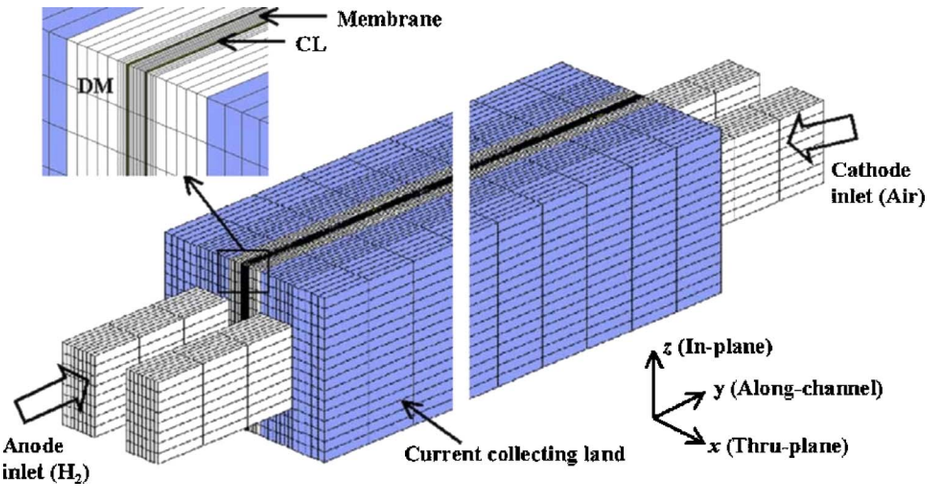

Figure 1. (Color online) Computational domain and mesh of a single-channel PEFC.

Table III. Cell geometry and parameters.

Description	Value
Cell length	70.0 mm
GC depth	0.5 mm
GC width	1.0 mm
Land width	1.0 mm
Anode/cathode DM thickness	0.210 mm
Anode/cathode CLs thickness	0.010 mm
Porosity of anode/cathode DM, ε_{DM}	0.6
Porosity of anode/cathode CLs, ε_{CL}	0.6
Volume fraction of ionomer in anode/cathode CLs, ε_e	0.18
Permeability of anode/cathode DM, K_{DM}	3.0×10^{-12} m^2
Hydraulic permeability of membrane, K_{mem}	5.0×10^{-20} m^2
Electronic contact resistance between CL and DM, R_{CDM}	1.0×10^{-6} Ω m^2
Anode/cathode inlet pressure, P_{in}	1.5 atm
Cell temperature, T_{cell}	80°C
Anode/cathode stoichiometry, ξ_a/ξ_c	2/2
Anode/cathode inlet humidification at 80°C, RH_a/RH_c	75%/75%
Catalyst coverage coefficient, n_c (assumed)	2.0
Diffusivity correction factor, n (assumed)	2.3

DM/CL interfaces are shown in Fig. 3 for three different membrane thicknesses at 1.5 A/cm^2 where no droplet coverage at DM/DC interface is assumed, because the gas flow rate in the channel is sufficiently high at the high current density of 1.5 A/cm^2 to remove water droplets efficiently from the DM surface.[13,21,22] First, it is observed that the accumulation of liquid water inside the DM is higher under the land area than the channel area, indicating that the liquid water is removed to the dryer gas flow from the channels. Second, the membrane thickness has a significant influence on the liquid water distribution within the anode and cathode DMs. The thicker membrane has a higher resistance to water diffusion and hydraulic permeation through it and thus allows less transport of water into the anode side. As a result, most of the liquid water is located on the cathode DM with the thickest membrane (108 μm), while liquid water is almost evenly distributed in both the anode and cathode DMs with 18 μm membrane.

Figure 4 displays the liquid saturation profiles in the anode and cathode DMs on the plane cutting across the center of channels and lands, respectively, for the same three cases. Similarly, liquid water is more evenly accumulated in both anode and cathode DMs with the thinner membrane, and the cathode DM under the lands is more flooded than under the channels. In addition, the variations of liquid water along the flow path, particularly at the center of channels, clearly show main characteristics of the liquid saturation profile in

Table IV. Physical properties.

Description	Value
Exchange current density—Ratio of reaction surface to CL volume in anode side, $ai_{0,a}^{ref}$	1.0×10^9 A/m^3
Exchange current density—Ratio of reaction surface to CL volume in cathode side, $ai_{0,c}^{ref}$	2.0×10^4 A/m^3
Reference hydrogen molar concentration, $c_{H_2,ref}$	40.88 mol/m^3
Reference oxygen molar concentration, $c_{O_2,ref}$	40.88 mol/m^3
Anodic and cathodic transfer coefficients for hydrogen oxidation reaction (HOR)	$\alpha_a = \alpha_c = 1$
Cathodic transfer coefficient for oxygen reduction reaction (ORR)	$\alpha_c = 1$
Dry membrane density, ρ^{mem}	2000 kg/m^3
Equivalent weight of electrolyte in membrane, *EW*	1.1 kg/mol
Faraday Constant, *F*	96487 C/mol
Universal Gas Constant, R_u	8.314 J/mol K
Surface tension, σ	0.0625 N/m
Liquid water density, ρ^l (80°C)	972 kg/m^3
Liquid water viscosity, μ^l	3.5×10^{-4} N s/m^2
Contact angle of anode/cathode DM and CLs, θ	92°
Effective electronic conductivity in CLs, σ_{CL}	1000 S/m
Effective electronic conductivity in DM, σ_{DM}	10000 S/m
Electronic conductivity in current collector, σ_{land}	20000 S/m

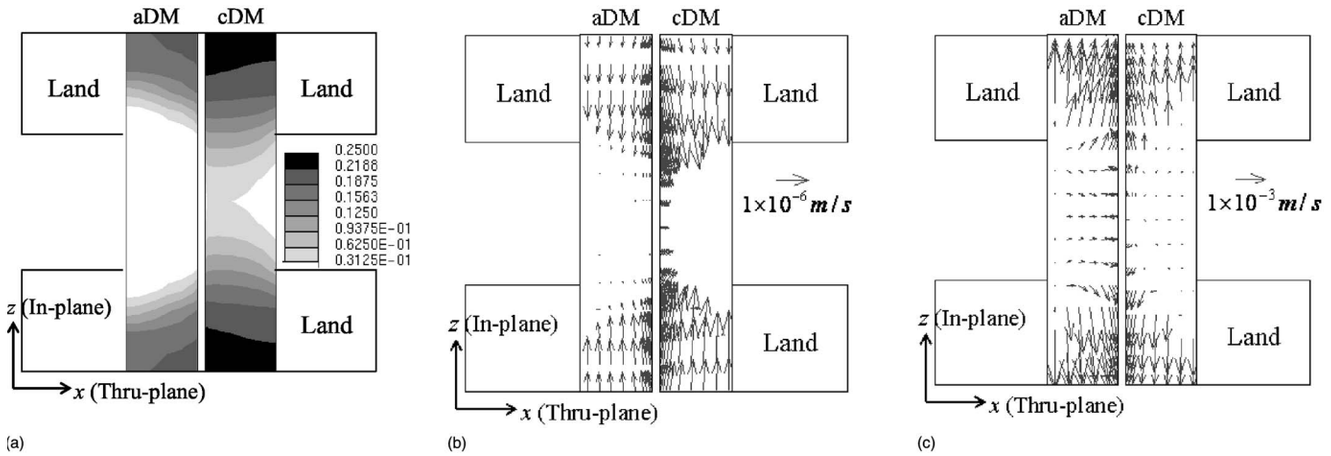

Figure 2. (a) Liquid saturation and (b) liquid and (c) gas velocity fields in the cross-section of the anode/cathode DMs at the fractional distance from cathode inlet of 0.1: I = 1.5 A/cm^2, δ_{mem} = 18 μm.

counter-flow with low-humidified inlets. Near the inlets, the evaporation front is located in the vicinity of the CL reaction area due to the low-humidified inlet feed gases. Then, once more water is produced by ORR and condensed along the cathode flow path, the two-phase zone broadens, pushing the evaporation front towards the DM/GC interface. However, the two-phase zone shrinks near the cathode outlet, which coincides with the dry anode inlet in the counter-flow cell. Water from the cathode is transported through the membrane towards the dry anode. Therefore, the peak of liquid water is located near the middle of the flow path under the counter-flow configuration of low-humidity cells.

Figure 5 displays two-dimensional distributions of the total water mass as calculated by Eq. 41. These contours are directly comparable with two-dimensional NR experimental data. Besides the water mass under the land area exceeding that in the channel area, it is observed that the total water mass greatly increases with increasing membrane thickness. For instance, the maximum water mass in the case of 108 μm membrane is around 11 mg/cm^2, much higher than the maximum water mass of 7 mg/cm^2 in the case of 18 μm membrane. This fact implies that with the thick membrane, the amount of water mass accumulated in the electrolyte phase is significant and exceeds the amount of water mass accumulated inside the two DMs.

The diagram in Fig. 6 further shows the water mass averaged under the land area of the entire cell, and its breakdown into the anode DM, cathode DM, and the electrolyte from the membrane and CLs, respectively. First, it is more clearly seen in Fig. 6 that the amount of water mass in the electrolyte significantly increases with increasing membrane thickness, while the water accumulation in the anode DM decreases and that in the cathode DM increases. Second, note that with the thinnest membrane (18 μm membrane), the water mass in the electrolyte phase (1.31 mg/cm^2) is still not negligible, taking around 20% of the total water (6.78 mg/cm^2), which indicates that the water mass in the electrolyte phase should not be overlooked in NR data processing for any membrane thickness. Third, the result shown in Fig. 6 indicates an inherent difficulty detecting liquid water in the cathode DM separately from the total NR water. For instance, if a thin membrane, such as the 18 μm thick membrane here, is employed in NR experiments, a significant amount of liquid water can be accumulated in the anode DM as well, resulting in the difficulty characterizing the liquid water in the cathode DM alone. On the contrary, using thicker membranes like the 108 μm membrane enables us to exclude liquid water in the anode side (here, 0.847 mg/cm^2 or 8% of the total water) but introduces the huge amount of water in the electrolyte phase (6.29 mg/cm^2 or 61% of the total water). Therefore, the possibility of estimating the amount of liquid water within the cathode DM by NR remains elusive.

Figure 7 shows the liquid saturation contours at the anode and cathode DM/CL interfaces at 0.5 A/cm^2 current density with the 54 μm membrane. Two cases are considered in Fig. 7: no interfacial coverage of liquid water on the cathode DM surface (Fig. 7a) and 18% interfacial coverage (Fig. 7b) to account for the presence of water droplets on the DM surface at lower gas velocities. While the assumed value of 18% interfacial coverage is arbitrary here in order to investigate the effect of interfacial coverage on the liquid saturation profile and total water mass distribution, ample experimental observations did indicate that droplet formation and removal on the cathode DM surface strongly depend on the gas flow rate in the channel.[20-22] Comparing Fig. 7a and b, the presence of liquid water coverage on the cathode DM surface significantly influences the amount of liquid water under the channel area, while the land area is relatively insensitive. For instance, at the cathode CL/DM interface, 0.06 increase in liquid water saturation is predicted under the channel area but only 0.02 increase under the land area with the 18% liquid interfacial coverage. However, it should not be overlooked that if the channel flooding becomes severe, the large liquid droplet coverage induced by the high channel flooding may significantly alter the level of DM flooding in the land areas. Meng and Wang[13] already elucidated the physical aspect where DM flooding is likely determined by the interfacial phenomena with severe channel flooding (i.e., high droplet coverage).

Figure 8 compares the total water mass distributions for the two cases discussed above where higher total water mass is observed with liquid interfacial coverage, showing roughly 1 mg/cm^2 difference under the land area and 2 mg/cm^2 difference under the channel area. When Fig. 8a is compared with Fig. 5b where no interfacial coverage is assumed for both high and low current density cases, the total water accumulation becomes lower with the lower current density (0.5 A/cm^2) due to the lower water production rate. On the other hand, considering interfacial droplet coverage, the water mass under the two different current densities can be compared between Fig. 8b and Fig. 5b. It is seen that the total water mass at 0.5 A/cm^2 is still lower under the land area but becomes higher under the channel area due to the droplet coverage at the cathode DM/GC interface. Therefore, the presence of interfacial coverage at 0.5 A/cm^2 diminishes the difference in the total water mass (both channel and land areas included) between 1.5 and 0.5 A/cm^2. This fact may well explain the trend typically observed in NR experi-

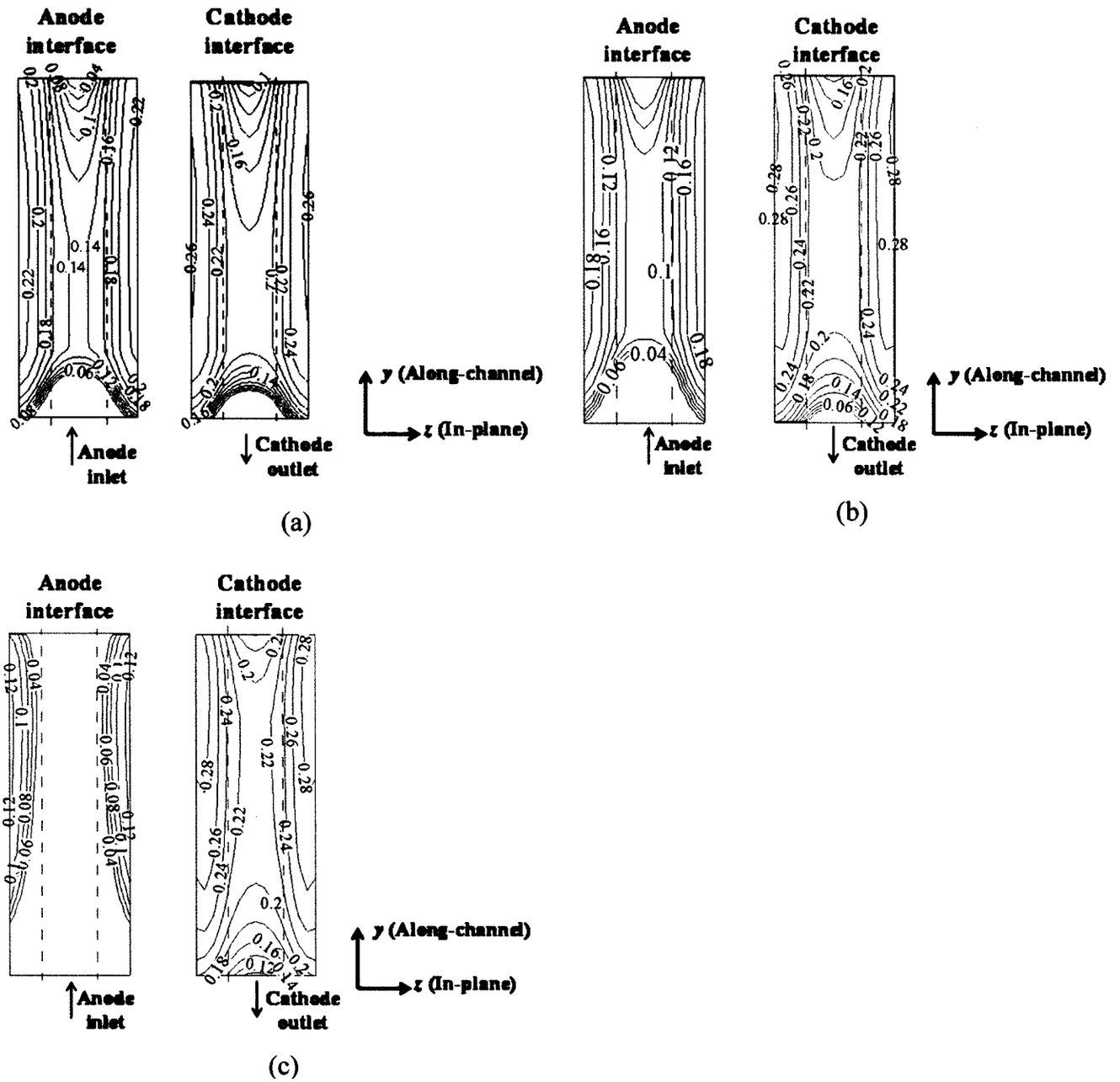

Figure 3. Liquid saturation contours at the DM/CL interfaces for different membrane thicknesses: (a) 18, (b) 54, and (c) 108 μm at I = 1.5 A/cm^2. The two dashed lines in each contour plot represent the channel-land boundaries.

ments where the total water accumulation does not necessarily increase with the current density but rather becomes nearly constant with increasing current density.[27-29] In addition, it should be pointed out that the results of total water mass shown in Fig. 5, 6, and 8, predicted by the current two-phase PEFC model, range from 7 to 11 mg/cm^2 (or roughly 70 to 110 μm water film thickness), which is in good agreement with NR data reported in the literature.[27,28] More importantly, it is now clear that high uncertainties may arise when interpreting NR data by invoking gross assumptions that are not carefully justified.

A simple way to estimate liquid water in the cathode DM from total NR water is given below. Consider NR data taken under the land area only which involves no complexity of channel water. Then the total water mass, wm_t, consists of two parts, water accumulation in the electrolyte, wm_e, and in the two DMs, wm_{DM}; i.e., $wm_t = wm_e + wm_{DM}$. The water mass in the electrolyte phase can be estimated from the membrane thickness, δ_{mem}, CL thickness, δ_{CL}, and ionomer fraction of CL, ε_e, as follows

$$wm_e = M_w \frac{\rho^{mem}\lambda}{EW}(\delta_{mem} + 2\varepsilon_e\delta_{CL}) \qquad [42]$$

For the 18 μm membrane, this is

$$wm_e = 0.018\frac{2000 \times 14}{1.1}(18 + 2 \times 0.18 \times 10) \times 10^{-4}$$
$$= 1.00 \text{ mg/cm}^2$$

Similarly for the 108 μm membrane, one has

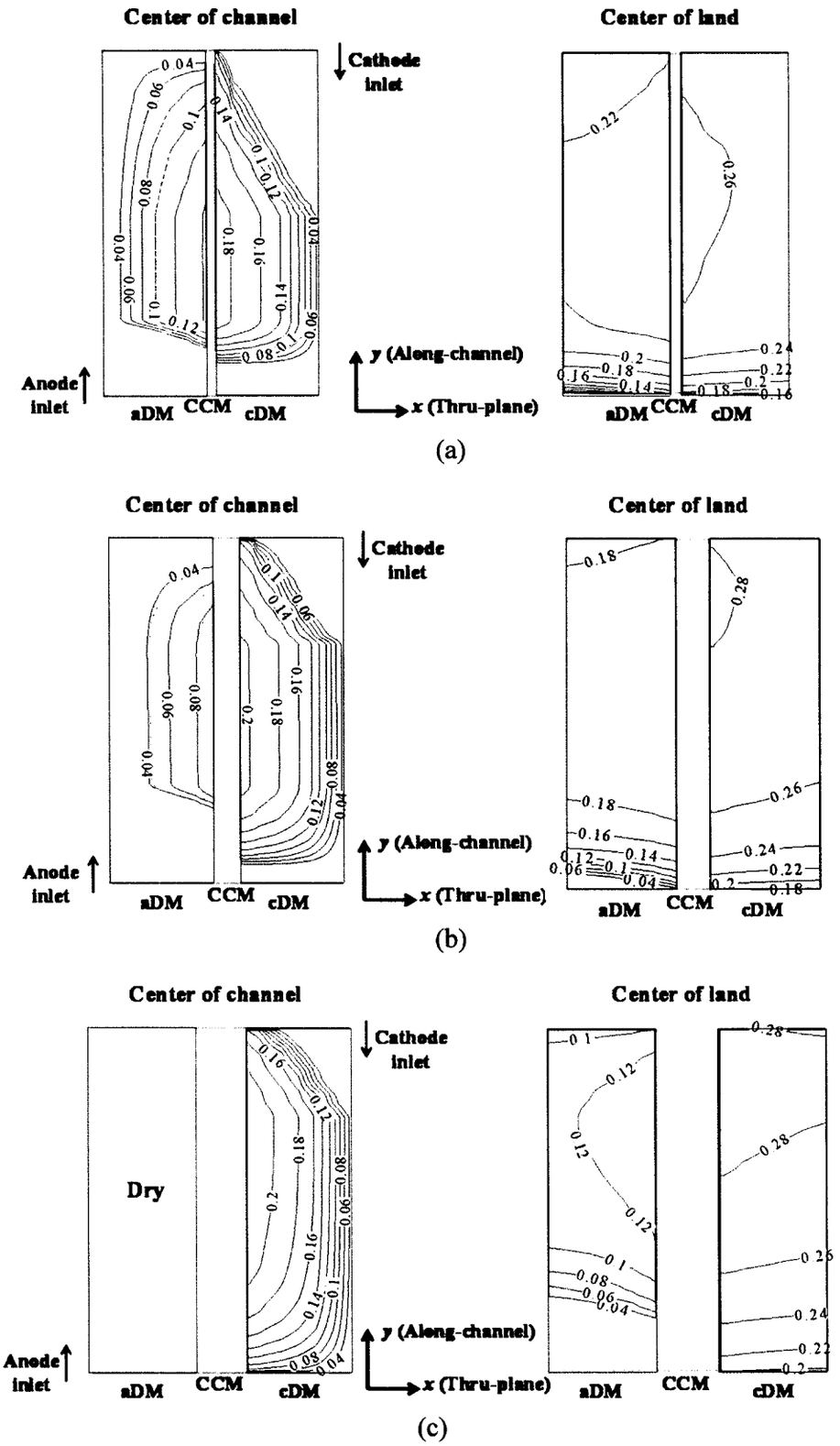

Figure 4. Liquid saturation contours in DMs cutting across the center of channels and lands for different membrane thicknesses: (a) 18, (b) 54, and (c) 108 μm at I = 1.5 A/cm^2.

$$wm_e = 0.018\frac{2000 \times 14}{1.1}(108 + 2 \times 0.18 \times 10) \times 10^{-4}$$
$$= 5.11 \text{ mg/cm}^2$$

where overall water content, λ is assumed to be that in equilibrium with saturated water vapor (i.e., λ = 14), a lower bound in the two-phase situation considered here.

On the other hand, water mass in the anode and cathode DMs can be approximated as follows

$$wm_{DM} = \varepsilon\rho^l s\delta_{DM} + \varepsilon\rho^g m_w^g(1 - s)\delta_{DM} \approx \varepsilon\rho^l s\delta_{DM} \quad [43]$$

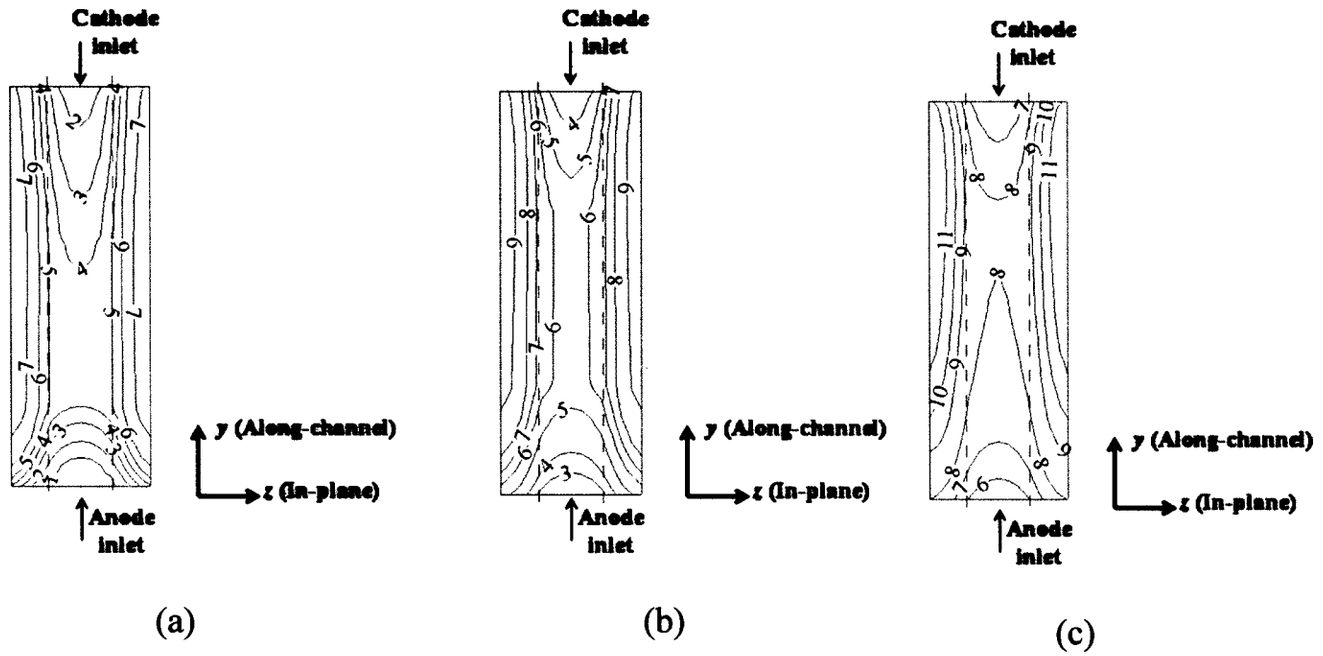

Figure 5. Total water mass, (mg/cm^2) distribution for different membrane thicknesses: (a) 18, (b) 54, and (c) 108 μm at I = 1.5 A/cm^2.

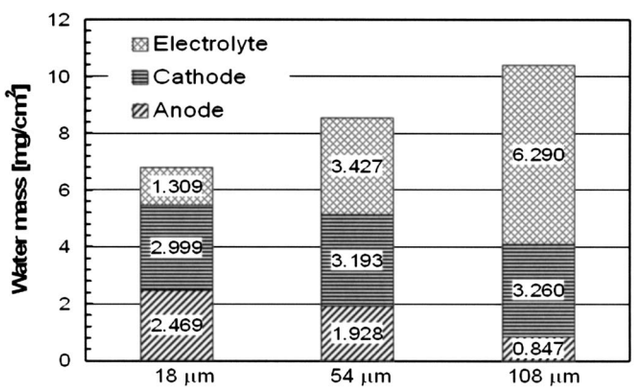

Figure 6. Average amounts of water mass over the land area in the anode DM, cathode DM, and electrolyte phase.

Thereafter, the calculated water mass for the electrolyte phase above is subtracted from the total water mass to estimate liquid water in the two DMs. For example, using the numerical NR data given in Fig. 6 which were taken under the land area (7 mg/cm^2 for the 18 μm membrane and 10.5 mg/cm^2 for the 108 μm membrane), the water mass in the two DMs is calculated to be 6.0 and 5.39 mg/cm^2 for the 18 μm and 108 μm membranes, respectively.

In the case of the thin membrane (18 μm), it is reasonable to assume that a similar amount of liquid water exists in anode and cathode DMs, rendering roughly 24.5% liquid saturation in each of DMs. That is

$$s_{DM} = \frac{wm_{DM}}{2\varepsilon\rho^l\delta_{DM}} = \frac{6.0}{2 \times 972\ \text{kg/m}^3 \times 210\ \mu\text{m} \times 0.6} = 24.5\%$$

On the other hand, if assuming liquid water exists only in the cathode DM, though very unlikely for such a thin membrane, 49% liquid saturation results. That is

$$s_{DM} = \frac{wm_{DM}}{\varepsilon\rho^l\delta_{DM}} = \frac{6.0}{972\ \text{kg/m}^3 \times 210\ \mu\text{m} \times 0.6} = 49\%$$

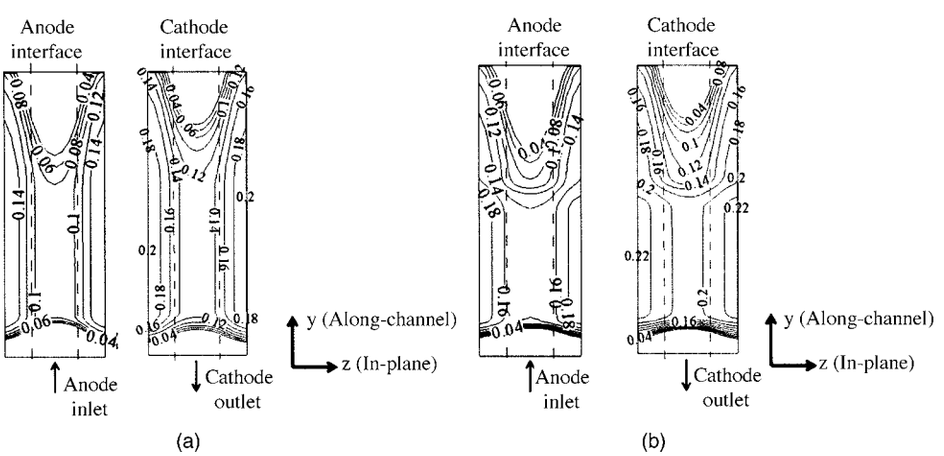

Figure 7. Liquid saturation contours at the DM/CL interfaces at I = 0.5 A/cm^2 for 54 μm thick membrane: (a) w/o liquid interfacial coverage, (b) with 18% liquid interfacial coverage at the cathode DM/GC interface. The two dashed lines in each contour plot represent the channel-land boundaries.

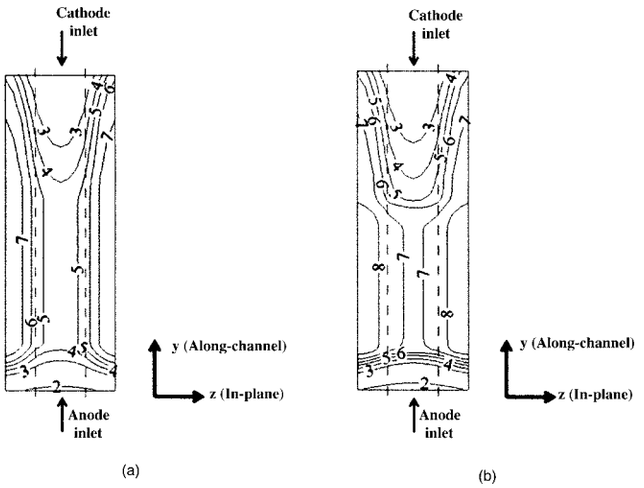

Figure 8. Total water mass (mg/cm^2) distributions at $I = 0.5$ A/cm^2 for 54 μm thick membrane: (a) without liquid interfacial coverage, (b) with 18% liquid interfacial coverage at the cathode DM/GC interface. The two dashed lines in each contour plot represent the channel-land boundaries.

The level of cathode DM flooding in reality should lie between these two limits, but leaning more towards the low limit (24.5%). Similarly, liquid saturation in the cathode DM for the thicker membrane case (108 μm) is estimated between 44% and 22%.

Conclusions

A numerical study was performed to assess the possibility of evaluating cathode DM flooding from NR water measurements. The following conclusions can be drawn:

The current two-phase PEFC model predicts the NR water, averaged through the cell thickness, ranging from 7 to 11 mg/cm^2 (i.e., approximately 70 to 110 μm water film thickness). This is in good agreement with NR data published in the literature, thus demonstrating the validity of the present two-phase model.

Simulation results reveal an inherent difficulty in separating the cathode water from anode water in the NR water data in the case of thin membranes.

In the case of thick membranes, the difficulty lies in separating cathode water from that in the electrolyte.

By including liquid interfacial coverage at the cathode DM surface, the two-phase model predicts the total water mass depending weakly on the current density, in qualitative agreement with the NR experimental observations. This underscores the necessity to consider interfacial coverage in two-phase models, particularly under low current density and low stoichiometry situations.

The inability of NR to separate cathode water from anode water suggests caution in its use for studying water management issues where water balance between the anode and cathode must be resolved. More elaborative considerations in interpreting NR data should be exercised and other alternatives to NR, such as MRI and X-ray tomography,[41] may be necessary. Finally, the liquid water distributions across the DM thickness, critically required for a rigorous validation of two-phase modeling, are still absent in the literature.

Acknowledgments

Financial support of this work by General Motors is gratefully acknowledged. C.Y.W. also acknowledges partial support from NSF grant no. 0609727.

The Pennsylvania State University assisted in meeting the publication costs of this article.

List of Symbols

a	water activity or effective catalyst area per unit of total volume, m^2/m^3
A	area, m^2
C	molar concentration, mol/m^3
D_k	mass diffusivity of species k, m^2/s
EW	equivalent weight of dry membrane, kg/mol
F	Faraday constant, 96487 C/mol
i_0	exchange current density, A/m^3
j	transfer current density, A/m^3
J	Leverett function
k_r	relative permeability
K	hydraulic permeability, m^2
M	molecular weight, kg/mol
m	mass fraction
n	number of electrons in electrochemical reaction or diffusivity correction factor
n_c	catalyst coverage coefficient
n_d	electro-osmotic drag coefficient
P	pressure, Pa
P_c	capillary pressure, Pa
R_{CDM}	contact resistance between CL and DM, Ω m^2
RH	inlet relative humidification
R_u	universal gas constant, 8.314 J/(mol K)
s	stoichiometry coefficient in electrochemical reaction or liquid saturation
S	source term in transport equation
t	time, s
T	temperature, K
u	fluid velocity and superficial velocity in porous medium, m/s
U_o	thermodynamic equilibrium potential, V
V	volume, m^3
V_{cell}	cell potential, V
wm	water mass, mg/cm^2

Greek

δ_i	thickness of component i
ε	volume fraction of gaseous phase in porous region
ε_e	volume fraction of ionomer phase in CL
γ	advection correction factor membrane water content, mol H_2O/mol SO_3^-
λ^α	relative mobility of phase α phase potential, V overpotential, V
θ	contact angle, °
μ	viscosity, kg/(m s)
ρ	density, kg ‖ m^3
ρ^{mem}	dry membrane density, kg/m^3
υ	kinematic viscosity, m^2/s
σ	surface tension, N/m or electronic conductivity, S/m viscous shear stress, N/m^2 ionic conductivity, S/m
ξ	stoichiometry flow ratio

Superscripts

e	electrolyte
eff	effective value in porous region
mem	membrane
g	gas
l	liquid
ref	reference value
sat	saturation value

Subscripts

a	anode
avg	average value
c	cathode
CL	catalyst layer
DM	diffusion medium
e	electrolyte
g	gas phase
GC	gas channel
H_2	hydrogen
i	species index
in	channel inlet
m	mass equation
mem	membrane
N_2	nitrogen
O_2	oxygen
ref	reference value
t	total

s	solid
sat	saturation value
w	water
Φ	potential equation
0	standard condition, 298.15 K and 101.3 kPa (1 atm)

References

1. Z. H. Wang, C. Y. Wang, and K. S. Chen, *J. Power Sources*, **94**, 40 (2001).
2. D. Natarajan and T. V. Nguyen, *J. Electrochem. Soc.*, **148**, A1324 (2001).
3. S. Mazumder and J. V. Cole, *J. Electrochem. Soc.*, **150**, A1510 (2003).
4. J. H. Nam and M. Kaviany, *Int. J. Heat Mass Transfer*, **46**, 4595 (2003).
5. T. Berning and N. Djilali, *J. Electrochem. Soc.*, **150**, A1589 (2003).
6. U. Pasaogullari and C. Y. Wang, *J. Electrochem. Soc.*, **151**, A399 (2004).
7. U. Pasaogullari and C. Y. Wang, *Electrochim. Acta*, **49**, 4359 (2004).
8. A. Z. Weber, R. M. Darling, and J. Newman, *J. Electrochem. Soc.*, **151**, A1715 (2004).
9. J. Yuan and B. Sunden, *Electrochim. Acta*, **50**, 677 (2004).
10. G. Lin, W. He, and T. V. Nguyen, *J. Electrochem. Soc.*, **151**, A1999 (2004).
11. U. Pasaogullari and C. Y. Wang, *J. Electrochem. Soc.*, **152**, A380 (2005).
12. U. Pasaogullari, C. Y. Wang, and K. S. Chen, *J. Electrochem. Soc.*, **152**, A1574 (2005).
13. H. Meng and C. Y. Wang, *J. Electrochem. Soc.*, **152**, A1733 (2005).
14. C. Ziegler, H. M. Yu, and J. O. Schumacher, *J. Electrochem. Soc.*, **152**, A1555 (2005).
15. E. Birgersson, M. Noponen, and M. Vynnycky, *J. Electrochem. Soc.*, **152**, A1021 (2005).
16. A. Z. Weber and J. Newman, *J. Electrochem. Soc.*, **152**, A677 (2005).
17. Y. Wang and C. Y. Wang, *J. Electrochem. Soc.*, **153**, A1193 (2006).
18. Y. Wang, Ph.D. Thesis, The Pennsylvania State University, University Park, PA (August 2006).
19. C. Y. Wang, *Chem. Rev. (Washington, D.C.)*, **104**, 4727 (2004).
20. K. Tüber, D. Pócza, and C. Hebling, *J. Power Sources*, **124**, 403 (2003).
21. X. G. Yang, F. Y. Zhang, A. L. Lubawy, and C. Y. Wang, *Electrochem. Solid-State Lett.*, **7**, A408 (2004).
22. F. Y. Zhang, X. G. Yang, and C. Y. Wang, *J. Electrochem. Soc.*, **153**, A225 (2006).
23. A. Hakenjos, H. Muenter, U. Wittstadt, and C. Hebling, *J. Power Sources*, **131**, 213 (2004).
24. X. Liu, H. Guo, and C. Ma, *J. Power Sources*, **156**, 267 (2006).
25. R. J. Bellows, M. Y. Lin, M. Arif, A. K. Thompson, and D. Jacobson, *J. Electrochem. Soc.*, **146**, 1099 (1999).
26. R. Satija, D. L. Jacobson, M. Arif, and S. A. Werner, *J. Power Sources*, **129**, 238 (2004).
27. D. Kramer, J. Zhang, R. Shimoi, E. Lehmann, A. Wokaun, K. Shinohara, and G. G. Scherer, *Electrochim. Acta*, **50**, 2603 (2005).
28. J. Zhang, D. Kramer, R. Shimoi, Y. Ono, E. Lehmann, A. Wokaun, K. Shinohara, and G. G. Scherer, *Electrochim. Acta*, **51**, 2715 (2006).
29. M. A. Hickner, N. P. Siegel, K. S. Chen, D. N. McBrayer, D. S. Hussey, D. L. Jacobson, and M. Arif, *J. Electrochem. Soc.*, **153**, A902 (2006).
30. N. Pekula, K. Heller, P. A. Chuang, A. Turhan, M. M. Mench, J. S. Brenizer, and K. Onlü, *Nucl. Instrum. Methods Phys. Res. A*, **542**, 134 (2005).
31. H. Ju, C. Y. Wang, S. Cleghorn, and U. Beuscher, *J. Electrochem. Soc.*, **152**, A1645 (2005).
32. C. Y. Wang and P. Cheng, *Int. J. Heat Mass Transfer*, **39**, 3607 (1996).
33. G. Luo, H. Ju, and C. Y. Wang, *J. Electrochem. Soc.*, Accepted.
34. R. B. Bird, W. E. Stewart, and E. N. Lightfood, *Transport Phenomena*, John Wiley & Sons, New York (1960).
35. R. E. Meredith and C. W. Tobias, in *Advances in Electrochemistry and Electrochemical Engineering 2*, C. W. Tobias, Editor, Interscience Publishers, New York (1962).
36. C. Berger, *Handbook of Fuel Cell Technology*, Prentice-Hall, New York (1968).
37. Y. Wang and C. Y. Wang, *J. Electrochem. Soc.*, **152**, 445 (2005).
38. T. E. Springer, T. A. Zawodinski, and S. Gottesfeld, *J. Electrochem. Soc.*, **138**, 2334 (1991).
39. *STAR-CD Version 3.15 methodology*, CD-Adapco Group (2001).
40. H. Ju, C. Y. Wang, S. Cleghorn, and U. Beuscher, *J. Electrochem. Soc.*, **153**, A249 (2006).
41. P. K. Sinha, P. Halleck, and C. Y. Wang, *Electrochem. Solid-State Lett.*, **9**, A344 (2006).